PERGAMON

Comparison of microwave radiative transfer calculations obtained with three different approximations of hydrometeor shape

Harald Czekala[a],*, Stephan Havemann[b], Karsten Schmidt[b], Tom Rother[b], Clemens Simmer[a]

[a]*Meteorological Institute, University of Bonn, Auf dem Hügel 20, 53121 Bonn, Germany*
[b]*German Aerospace Center, Kalkhorstweg 53, 17235 Neustreliz, Germany*

Abstract

The sensitivity of microwave radiative transfer through the atmosphere with respect to three different raindrop geometries (spheres, oblate spheroids and oblate raindrop shapes realistically approximated by a series of Chebyshev polynomials) is investigated with a one-dimensional numerical model. All rotational symmetric particles are aligned with their axis of rotation along the vertical. Single-scattering calculations are performed with an extended boundary condition T-matrix code provided by Mishchenko and the Discretized Mie Formalism. In contrast to the former code the latter allows to model the scattering by the Chebyshev-shaped raindrops. The change of brightness temperature when using one of the oblate particle shapes instead of the widely used spherical assumption reaches up to -5 K for 85 GHz at upward directions. The calculated microwave signatures are most sensitive to the shape of liquid water drops at frequencies around 20 GHz, while the results at 37 and 85 GHz show larger impact by ice particles. Polarization differences exhibit large changes when using oblate particle shapes instead of spheres, leading to changes of $+6$ K at upward and -15 K at downward directions. The slight variation of geometry when using Chebyshev shapes gives additional changes of -2 and $+4$ K at the same directions of emerging radiation. Calculations with an ice particle layer above the rain layer prove that the scattering signature of the underlying rain layer will not be screened by the ice particle scattering. This result shows the importance of correct treatment of raindrop shape even in the presence of large ice particles. © 1999 Elsevier Science Ltd. All rights reserved.

* Corresponding author. Tel.: $+49$-228-735-194; fax: $+49$-228-735-188
E-mail address: hczekala@uni-bonn.de (H. Czekala)

1. Introduction

Passive microwave (MW) observations of the earth's atmosphere (ground based, airborne and space borne) are widely used for the retrieval of meteorological data [1,2]. When considering clouds and precipitation, the radiation emitted by the surface and the atmosphere itself will be scattered, absorbed and emitted by the hydrometeors. The MW frequencies below 100 GHz (e.g. those used on the Special Sensor Microwave/Imager (SSM/I) operated from the Defense Meteorological Satellite Program (DMSP)) have a great potential for precipitation retrieval. On SSM/I the centre frequencies are 19.35, 22.235, 37.0, and 85.5 GHz, respectively. The Scanning Multifrequency Microwave Radiometer (SMMR) had additional channels at 6.6 and 10.7 GHz, which also are considered in this study because they will be used on the ADEOS-II satellite. Measurements at higher MW frequencies, as well as visible and infrared measurements, suffer from the effects of very high optical thickness and therefore are only able to obtain information from the upper or lower boundary of the cloud and rain events, depending on the location of the sensor, airborne or ground based.

The lowest MW frequencies have the capability to penetrate through the atmosphere without being fully absorbed. Even 3 km thick layers of moderate rain rates do not produce sufficient optical thickness to prevent radiation at 19.35 GHz from propagating from the surface to the top of the atmosphere. Thus these frequencies gather information along the whole path through the atmosphere rather than only from a boundary.

The retrieval scheme that links the observed intensity and polarization to physical parameters (such as temperature, humidity, rain rate, path integrated water or ice mass, etc.) is often set up by utilization of forward calculations. Numerical models are used to compute the MW radiation below, atop, and sometimes also within a well-defined atmosphere. The inversion of such calculations gives the retrieval algorithm. Obviously, the quality of the retrieval algorithm is directly connected to the accuracy of the physical model of the atmosphere on the one hand and the quality of the forward calculations on the other hand.

While the influence of certain surface conditions (at least for the sea surface) and the gaseous atmosphere on the radiation is quite well known and can be modelled with sufficient accuracy, the interaction with hydrometeors is still a problem. The MW radiation within clouds or precipitation is affected by the temperature (determining the refractive index for a certain frequency), phase, size distribution and shape of the hydrometeors. While some parameters cannot be modelled with the desirable accuracy due to the lack of knowledge of their behaviour in nature (e.g. the variability of the size distribution of rain is still a subject of ongoing research), other parameters raise practical problems in the formulation of the mathematical and numerical model that prevent their exact treatment.

Despite of the well-known fact that the shape of hydrometeors can be highly nonspherical, the interaction parameters are mostly calculated according to the Lorenz–Mie theory which assumes spherical shape. In case of liquid nonprecipitating cloud droplets this is a good approximation. Solid hydrometeors, that can be found in ice clouds, significantly differ from the spherical shape, but are small enough to fulfill the Rayleigh approximation for the frequencies under consideration: The size parameter $\chi = 2\pi r/\lambda$ (with r a typical particle dimension and λ the wavelength) and the real part n of the refractive index together obey the relations $\chi \ll 1$ and $n\chi \ll 1$, respectively [3]. In the case of Rayleigh scattering the shape is of no importance.

Precipitating liquid hydrometeors show significant deviation from spherical geometry, revealing complex (and mostly oblate) shapes that have been both modelled and measured [4–6]. In order to minimize the error of forward radiative transfer models (FRTM) there have been some approaches which use nonspherical particle shapes to approximate the realistic hydrometeor shapes [7–12]. A detailed discussion of this research topic can be found in the review paper by Haferman [13].

Microwave computations using realistic shapes for ice particles have been performed by some authors [14–17]. These studies mainly focus on cirrus clouds, but also consider large precipitating ice particles (hail stones, graupel). Insufficient knowledge on ice particle shape makes accurate modelling nearly impossible. Wu and Weinman used spheroid-shaped particles with their largest dimension aligned to the vertical [10]. The shape of raindrops falling at terminal velocity is far better known than the shape of hail. However, liquid precipitation is still handled by spheroid approximations rather than the more justified Chebyshev shapes that are derived from both, theoretical calculations [6] and experimental [18,5] data.

The subject of this paper is the comparison of radiative transfer results using three different assumptions on the shape of liquid and frozen precipitating hydrometeors (raindrops and hail stones). While the assumption of Chebyshev shape is a very realistic one for liquid drops, any assumption on the shape of hail stones is rather a guess than a good approximation. Therefore, the assumption of the same shape of hail and raindrops should be seen as a test of the general sensitivity of microwave signatures produced by hail to the particle shape which is used to model the scattering behaviour. The ice particle scattering results are not meant as a realistic calculation, but as a tool to investigate the screening of raining layers by additional ice particles above. We will demonstrate that even in the presence of a strongly scattering (and therefore depolarizing) ice particle layer, the raindrops still contribute to the total signal that may be measured from satellite radiometers, showing the importance of very accurate treatment of rain. To our knowledge this is the first time that the Chebyshev-approximated drop shapes are used in a FRTM and compared to other particle geometries.

In the following section we introduce the shapes (spheres, equivalent-volume oblate ellipsoids and the more realistical approximation by a series of Chebyshev polynomials). Section 3 gives an outline of the radiative transfer procedure, including the model description. A discussion of the results obtained for the different particle shapes is found in Section 4, followed by Section 5 which summarizes our conclusions.

2. Raindrop shapes

Only very small raindrops with diameters well below 1 mm are perfect spheres due to their high surface tension. Larger drops tend to be flattened at the bottom, leading to oblate shapes. When describing drop shapes, we refer to the work of Chuang and Beard [6,19], who used a dynamic model to study the behaviour of falling water drops. The influences of hydrostatic pressure, friction, surface tension and electric fields are taken into account, resulting in rotational symmetric shapes with cross sections $r = r(\theta)$ that can be described by a series of Chebyshev polynomials in $\cos(n\theta)$:

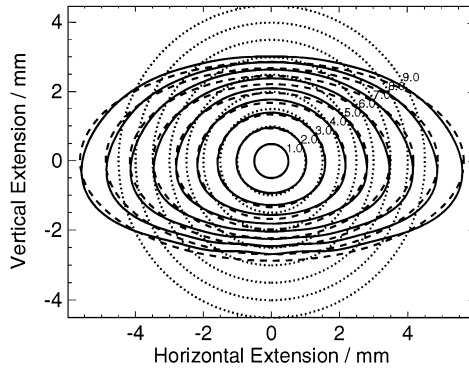$$r(\theta) = r_0\left(1 + \sum_{n=0}^{N} c_n \cos(n\theta)\right).$$ (1)

Fig. 1. Cross sections of falling drops (solid line) according to Chuang and Beard [6]. Equivalent volume spheres (dotted line) and spheroids (dashed line) with same aspect ratios give the approximated shapes.
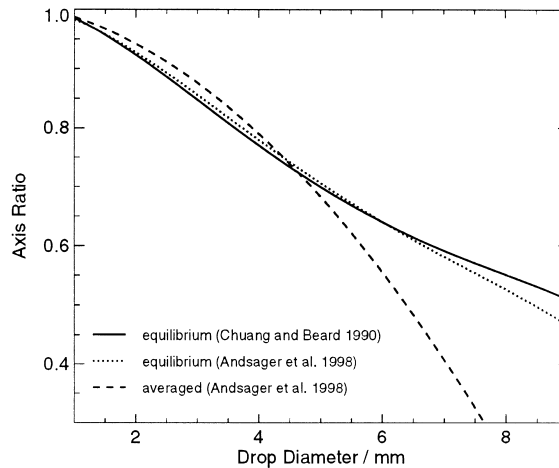

Fig. 2. Aspect ratio of falling drops: The modelled equilibrium shapes from Chuang and Beard [4] (solid line), the equilibrium drop shapes measured by Andsager et al. [20] (dotted line) and the averaged values for oscillating drops (dashed line, only valid below 4.1 mm, from Andsager et al. [20]).

The radius of the undistorted drop is given by r_0 and the coefficients c_n ($n = 0, 1, \ldots, 10$) for drop sizes from 1 to 9 mm diameter are taken from Chuang and Beard [6]. Resulting shapes are presented in Fig. 1, which also shows the cross sections of the corresponding spheres and spheroids of the same volume. It is clear from Fig. 1 that the spheres only give a poor approximation to the realistic drop shapes. The volume equivalent spheroids have the same aspect ratio as the corresponding Chebyshev drops and are used as another simplified drop shape in this study.

Flattening of the drops increases with larger diameters and is more pronounced at their bottom, leading to particles that do not exhibit a symmetry between upward and downward directions. In addition, large drops will start to oscillate around this shape due to vortex shedding and collisions with other large drops. At this stage we only consider equilibrium shapes.

The aspect ratio α of the Chebyshev particles, defined as the ratio of maximum vertical and horizontal extension, depends on the drop size $d = 2r_0$ (diameter in cm). It can be approximated with a fourth-order fit [6] to the numerical results

$$\alpha = 1.01668 - 0.98055d - 2.52686d^2 + 3.75061d^3 + 1.68692d^4 \tag{2}$$

and is plotted in Fig. 2 (solid line). Furthermore, we included the most recent results of Andsager et al. [20] in which aspect ratios were fitted to experimental results. The aspect ratio of equilibrium drop shapes (dotted line) and the average aspect ratio for oscillating drops (only fitted for diameters less than 4.1 mm) are very close to the model calculations.

3. Radiative transfer

3.1. Model description

The radiative transfer model used in this study is the one-dimensional model developed by Simmer [21] and recently extended by Czekala and Simmer [12,22] to include nonspherical scattering. The radiation is represented by the two-component Stokes vector $\bar{\mathbf{I}} = (I_v, I_h)$ of the vertically and horizontally polarized intensities. The reason for using only two components is that there is no coupling between the first and last two components of the Stokes vector due to the azimuthal symmetry of the problem under consideration.

The vector radiative transfer equation (VRTE)

$$\cos\theta \frac{d\bar{\mathbf{I}}(z,\theta)}{dz} = -\bar{\sigma}_e(z,\theta)\bar{\mathbf{I}}(z,\theta) + \bar{\sigma}_a(z,\theta)B(T(z)) + \int_0^\pi \bar{\bar{\mathbf{P}}}(z,\theta;\theta')\bar{\mathbf{I}}(z,\theta')\sin\theta'\,d\theta' \tag{3}$$

defines the differential change of polarized radiation with respect to vertical position z in scattering, emitting and absorbing media with particles of preferred orientation [23]. Extinction and absorption are described by the diagonal (2×2) matrix $\bar{\sigma}_e$ (which is used as a vector) and the two-element column vector $\bar{\sigma}_a$, where θ denotes the zenith angle of propagation direction, $T(z)$ the temperature at height z, $B(T)$ the temperature dependent emission according to Planck's law, and θ' the direction of incoming radiation that is scattered into the direction of propagation θ. The amount of scattered radiation is given by the (2×2) phase matrix $\bar{\bar{\mathbf{P}}}$. The VRTE is solved by the successive order of scattering (SOS) method.

Absorption by the atmospheric gases is calculated for molecular oxygen, nitrogen and water vapour according to the Millimeter Propagation Model (MPM) from Liebe [24,25] for a US-standard atmosphere. The upper boundary condition is set to 2.7 K cosmic background temperature, the lower boundary is modelled as a surface emitting with its corresponding temperature. The emissivity (ε) is either set to a fixed value or to the Fresnel reflection matrix of a calm water surface. In case of black body surface conditions or an Lambertian surface the surface temperature is the same as the sea surface temperature. The refractive index for water and ice is calculated as a function of temperature, frequency, phase (liquid or solid) and salinity [26]. Salinity and temperature for ocean water are set to 3.3 promille and 283.15 K, respectively.

3.2. Single scattering calculations

The interaction parameters $\bar{\sigma}_e$, $\bar{\sigma}_a$ and $\bar{\bar{\mathbf{P}}}$ may be calculated by three different methods: Spherical particles are, in general, treated with Lorenz–Mie theory [27]. For rotationally symmetric particles that have an additional symmetry to their plane of rotation (e.g. spheroids or particles described by only a single Chebyshev polynomial of even order) the extended boundary condition (EBC) T-matrix code from Mishchenko is used [28]. Furthermore, we have extended the FRTM to use the Discretized-Mie-Formalism (DMF), developed by Rother and Schmidt [29,30], for single-scattering calculations.

While the T-matrix implementation of Mishchenko in the current form is limited to scatterers having the additional mirror symmetry mentioned above, the DMF is able to handle any rotational symmetric object with a cross section that is given by a unique solution for $r = r(\theta)$ for each θ in the range from 0 to 180°. Particle shapes described by Chebyshev polynomials of odd order (as used by Wiscombe and Mugnai [31]) can therefore be treated with the DMF. Note that the DMF has been formulated so far for axisymmetric scatterers like spheroids, Chebyshev particles, finite circular cylinders and for infinitely extended noncircular cylinders. An extension to finitely approximated noncircular cylinders can be found in the study of Rother et al. [32].

Thus, we are able to perform passive microwave radiative transfer calculations which, for the first time, take into account the more realistic shape of raindrops described by a series of Chebyshev polynomials rather than a simpler approximation. For all calculations the rotational axis of the hydrometeors is aligned to the vertical.

The single-scattering calculations give solutions for the amplitude scattering function (ASF), which relates the scattered electromagnetic wave to the incident plane wave [23]. From the ASF we calculate the interaction parameters and integrate them over azimuth angle, ending up with the appropriate values for one-dimensional radiative transfer. Finally, we integrate the results for drops of a certain size and shape over a particle size distribution, obtaining the polydisperse scattering quantities in each model layer.

4. Results and discussion

For the calculations we used an atmospheric rain layer between the surface and 2 km height with three layers of different temperature. The polydisperse interaction parameters are computed with a Marshall–Palmer drop size distribution for a constant rain rate of 25 mm/h [33]. Some calculations have an additional layer of large, precipitating hail above the rain layer, reaching from 2 to 3 km. The aim of this atmospheric setup is to model realistic raindrop scattering on the one hand and the possible screening of these results by a hail layer above the rain on the other hand. The purpose of the ice layer is not to model real thunderstorm conditions, but to study the principle radiative transfer effects of such ice particle layers. For such a rough estimation the exact microphysical parameters are of minor importance; basic processes can be understood with these simple model assumptions. The size and shape distributions of the hail are not meant to be realistic in any other way than to produce a strong scattering signal: The nonspherical ice particles will lead to high polarization and depolarization efficiencies which modify the upwelling radiation emerging from the rain.
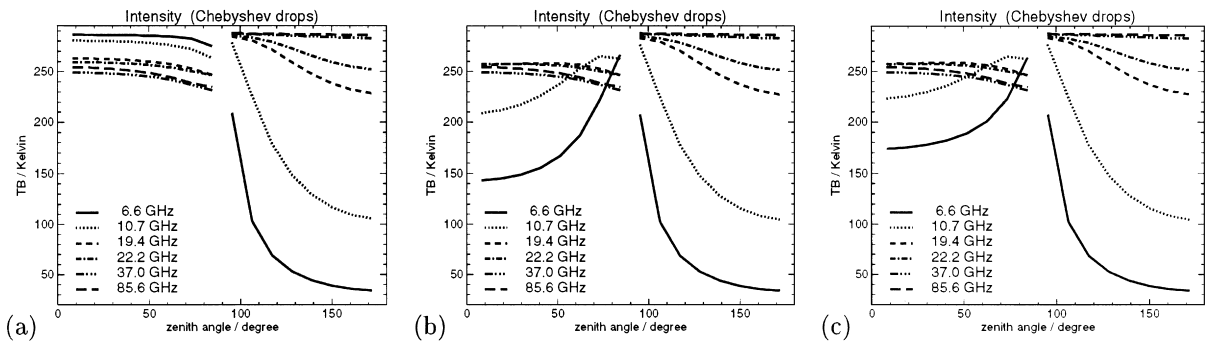
Fig. 3. Brightness temperature vs. zenith angle of propagation for six frequencies at 25 mm/h rain rate (no ice particles) and three different surface conditions: (a) black body emission ($\varepsilon = 1.0$), (b) sea surface (Fresnel), (c) lowered emissivity ($\varepsilon = 0.5$, Lambertian surface).

In order to determine the ice particle contribution alone the hail layer is calculated without the underlying rain layer. The comparison of the results for rain (without ice), ice (without rain), and rain (with ice) allows to estimate the screening effect of ice particles above rain layers. The results clearly state that the polarization signal produced by nonspherical raindrops emerges to the top of the atmosphere without being substantially attenuated.

Surface boundary effects were examined by using three different surface conditions: black body boundary condition ($\varepsilon = 1.0$), sea surface (using Fresnel reflection) and a fixed emissivity of $\varepsilon = 0.5$ (Lambertian surface). The latter case gives an enhanced angular variation of the radiation in the lower layers due to the reduced emissivity, which is very similar to the sea surface emission, but does not polarize the surface emission. This is useful for a separation between polarization effects that originate from either the highly polarized emission of a Fresnel surface or from the angular distribution of the intensity.

4.1. Intensity results

An example of the total radiation intensity (which is the sum of vertically (I_v) and horizontally (I_h) polarized intensity), expressed in terms of equivalent blackbody brightness temperatures, versus zenith angle of propagation is given in Fig. 3. Zero angle is the direction of upwelling radiation at nadir direction. At the horizontal direction (90°) the one-dimensional model is not defined.

The upwelling radiation at the high frequencies (37 and 85 GHz), which reach high opacities at 25 mm/h rain rate, are nearly unaffected by changes in the surface emission. The radiances are mostly determined by the temperature of the top of the raining layer. In the low-frequency regime the opacity is much lower, so that the reduced emissivities (polarized in Fig. 3b and unpolarized in Fig. 3c) lessen the nadir upwelling radiation. At angles close to the horizontal the path integrated optical thickness rises, leading to a saturation of the brightness temperatures at the physical temperature. Downwelling radiation results show the effect of optical thickness much stronger: At 85 GHz the radiation that can be observed at the bottom of the atmosphere comes only from the
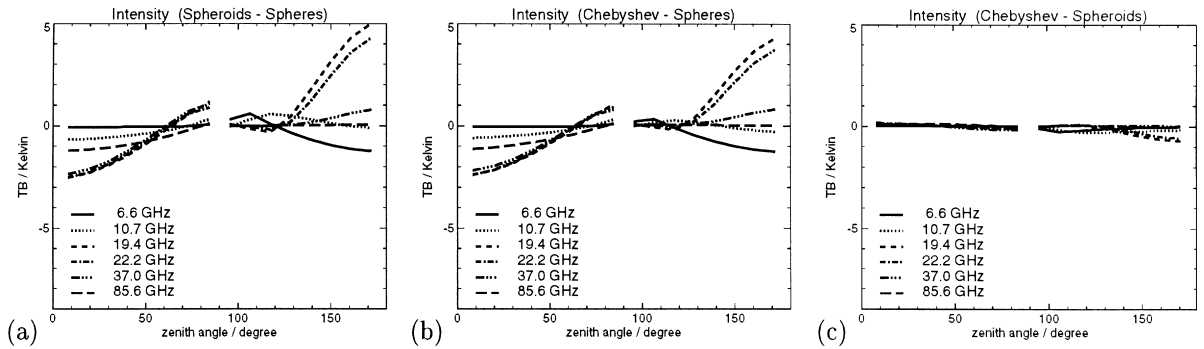
Fig. 4. Brightness temperature differences vs. zenith angle (rain only and blackbody emission at the surface): (a) Spheroids minus spheres, (b) Chebyshev drops minus spheres, (c) Chebyshev drops minus spheroids.
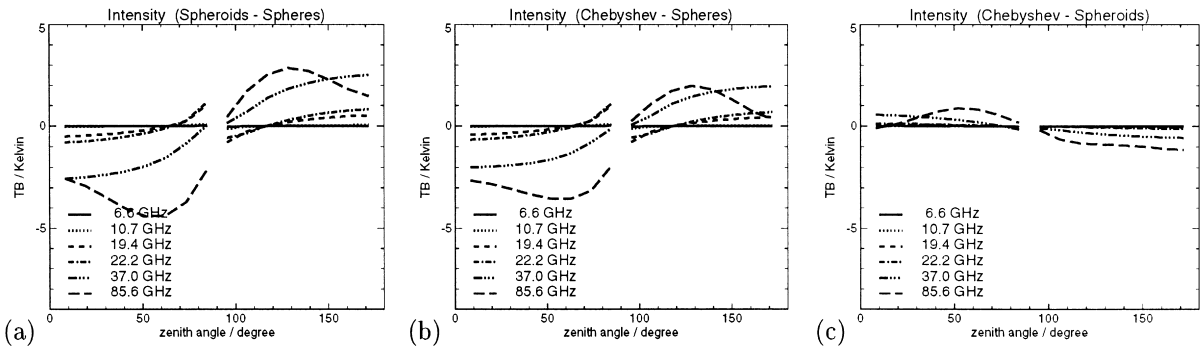

Fig. 5. All settings as in Fig. 4, but with the ice particle layer only (no rain).

lowest rain layers, leading to the highest brightness temperatures. At the lowest frequency of 6.6 GHz the atmosphere is very transparent resulting in a low emission by the atmosphere in addition to the cold background from space.

Fig. 4 shows the differences of calculations obtained with the three different assumptions on particle shape. A raining layer of oriented oblate particles (spheroids or Chebyshev drops) produces more radiation in downward directions and less radiation in upward directions (Figs. 4a and b). Since the results calculated with blackbody emission and fixed orientation of the particle are strongest for the low frequencies (22 and 37 GHz), this result indicates enhanced backscattering or emission for oblate particles compared to spheres. However, the difference between the spheroid approximation and the more realistic Chebyshev drops is minimal.

When considering only ice particle scattering (isolated from the corresponding rain layer), Fig. 5 clearly shows that the basic effect is the same, but this time more pronounced for larger frequencies. The 37 and especially the 85 GHz channel, which was very insensitive to the change of shapes for rain, exhibit remarkable changes of the intensity. At the latter frequency the spheroid shape suppresses additional 5 K of the upwelling radiation compared to spheres. The difference of
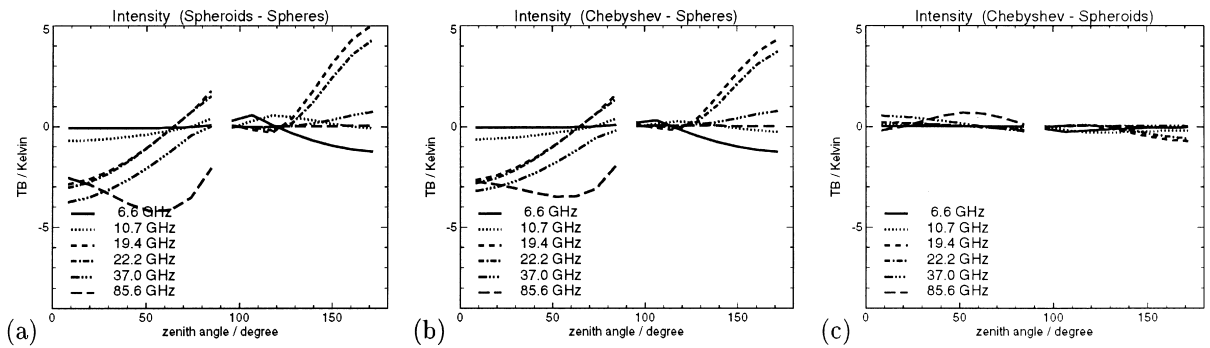
Fig. 6. All settings as in Fig. 4, but with the ice particle layer additional to the rain layer (both layers present).
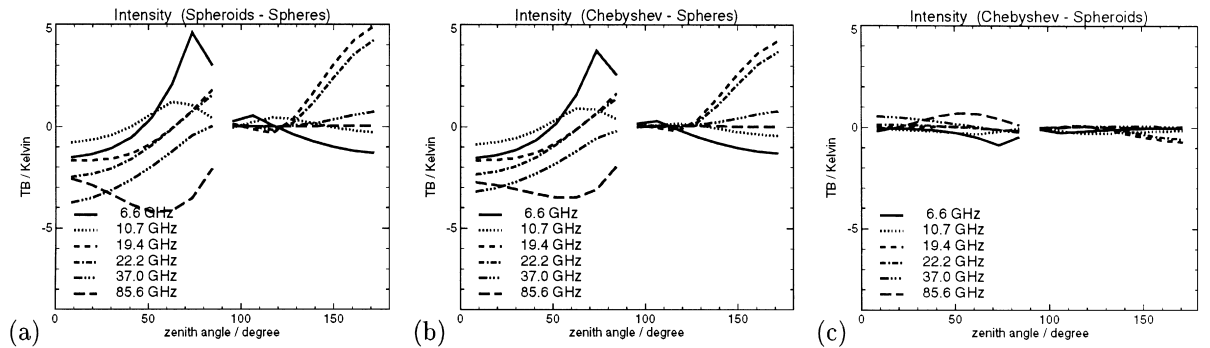

Fig. 7. All settings as in Fig. 6 (both layers, rain and ice), but with sea surface conditions at the lower boundary.

the two oblate shapes (Chebyshev minus spheroids, Fig. 5c) states that the Chebyshev-shaped particles lead to smaller changes in comparison to spheres.

Combining rain and ice layer in one calculation (Fig. 6) straightforward gives a 'mean' result from the single cases of Figs. 4 and 5. At upward directions the resulting differences for the low frequencies are fully determined by the raining layer and are not affected by ice particle scattering above. The opposite is true for 85 GHz, which has a significant sensitivity to ice particle scattering only. This separation of high and low frequencies is more difficult at 37 GHz, where the effects of both hydrometeor phases have an impact on the signal. The downwelling radiation is nearly the same as in the case of rain only because most of this radiation is emitted by the rain itself and may only interact with the liquid-phase hydrometeors on the path to the surface. Again, the differences between the spheroid shape and Chebyshev drops (Fig. 6c) are very small, giving a similar result as in the case of ice scattering only.

These results indicate a sensitivity of the low frequencies to changes in surface emission. Fig. 7 gives the results for the combination of rain and ice layer (as in Fig. 6), but with an underlying sea surface with reflection and emission according to Fresnel instead of a blackbody source. While the downwelling radiation is unaffected, there is a change for those frequencies with small opacity
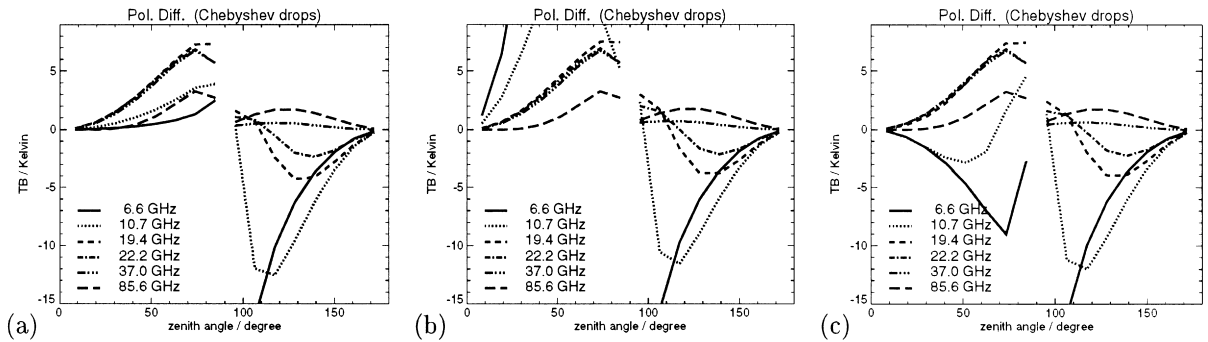
Fig. 8. PD vs. zenith angle of propagation for six frequencies at 25 mm/h rain rate (no ice particles) and three different surface conditions: (a) black body emission ($\varepsilon = 1.0$), (b) sea surface (Fresnel), (c) lowered emissivity ($\varepsilon = 0.5$). Note that the large PD values in (b) for a nearly transparent atmosphere are not connected to the hydrometeor shape, so that the results have been clipped.

which are able to see the surface from above the atmosphere. The channels at 6.6 and 10.7 GHz, which both were nearly unaffected by changes of particle shape in case of blackbody boundary conditions, now show larger differences, reaching from negative values (-1.5 K) to positive values ($+5$ K) depending on the angle.

4.2. Polarization results

The effect of scattering by hydrometeors is known to be twofold: On the one hand, the highly polarized radiation emanating from the sea surface is depolarized by the hydrometeors, and on the other hand, unpolarized radiation is polarized by the interaction process with liquid and frozen particles. The best-suited variable for remote sensing purposes is the polarization difference (PD), which is defined as the difference of vertically and horizontally polarized brightness temperature ($PD = T_{B,v} - T_{B,h}$). The total PD hence originates from two sources, which are the effects of hydrometeors on the one hand and the polarized emission by sea surface on the other hand.

Fig. 8 gives the resulting PD in case of the raining layer above three different surface types. While Figs. 8a and c include a nonpolarizing surface, Fig. 8b shows the high amount of linear polarization close to the Brewster angle for the low frequencies. Note that these large PD values for a nearly transparent atmosphere (at frequencies of 6.6 and 10.7 GHz and 25 mm/h rain rate) are not connected to the hydrometeor shape, so that the results have been clipped.

The effect of surface PD can be eliminated by subtracting calculations performed with spherical particles from those with Chebyshev drop shapes (Fig. 9). The PD of the upwelling radiation at low frequencies and blackbody surface emission (Fig. 9a) differs from the two surface conditions with a lower emissivity. These two calculations (Figs. 9b and c) have similar emissivities, but completely different polarization features. However, the resulting PD matches almost perfectly.

The comparison of the different shapes is done in Fig. 10, restricting the results to only those calculations with surface emissivity $\varepsilon = 1.0$. As for the total intensity, the results for the PD are very similar (Fig. 10c) for the two oblate shapes, which both show large differences to the spherical shape. The low-frequency range, which produces the largest positive change in PD of up to $+5$ K
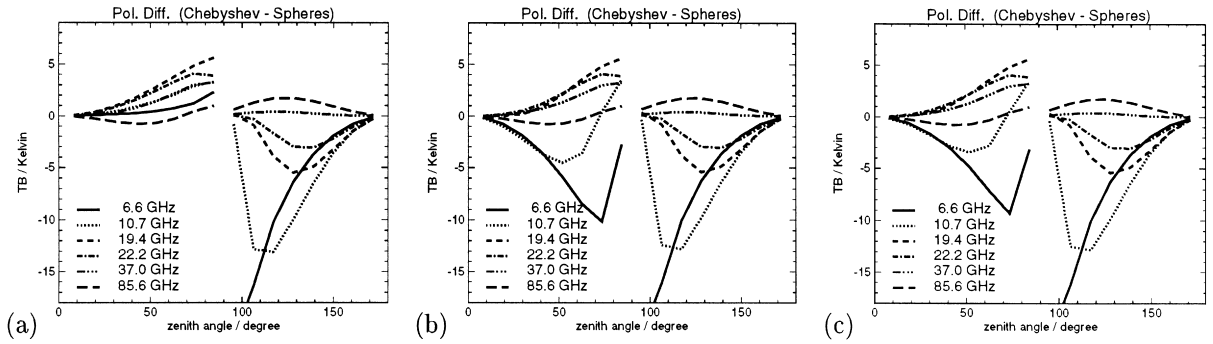
Fig. 9. Difference of PD difference (Chebyshev drops minus spheres) vs. zenith angle of propagation for three different surface conditions: (a) black body emission ($\varepsilon = 1.0$), (b) sea surface (Fresnel), (c) lowered emissivity ($\varepsilon = 0.5$).
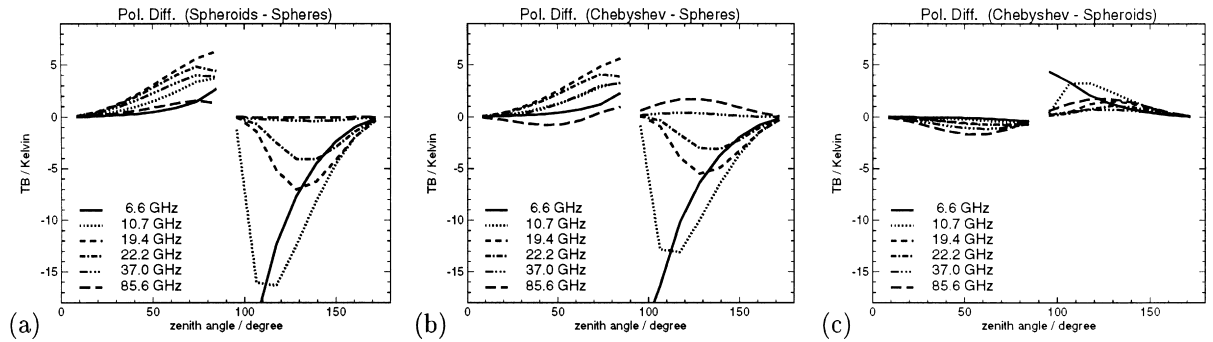

Fig. 10. PD differences vs. zenith angle (rain only and blackbody emission at the surface): (a) Spheroids minus spheres, (b) Chebyshev drops minus spheres, (c) Chebyshev drops minus spheroids.

when switching to oblate shapes is not sensitive to the small deviation in particle geometry between spheroids and Chebyshev particles. Only the 85 GHz channel, which has a positive (but small) PD for spheroids changes to small negative values. The PD of downwelling radiation is more sensitive to small changes of the particle shape: Chebyshev drops produce about max. 4 K less negative PD (which gives a positive change) than the spheroid particles. In general, the main findings for PD are similar to the findings for total intensity: The more realistic Chebyshev particles show on the large scale very similar results to the spheroids, but somewhat less changes compared to spheres than the spheroids.

When considering ice particle scattering by the single layer with hail, the trend of the calculation with rain only is reproduced. The PD at upward directions is increased (e.g. + 10 K for 37 GHz) when either spheroids (Fig. 11a) or Chebyshev particles (Fig. 11b) are used instead of spheres. At opposite direction of propagation, oblate particles produce a smaller PD. The Chebyshev shapes reduce the changes at 37 GHz originating from the use of spheroids (Fig. 11c).
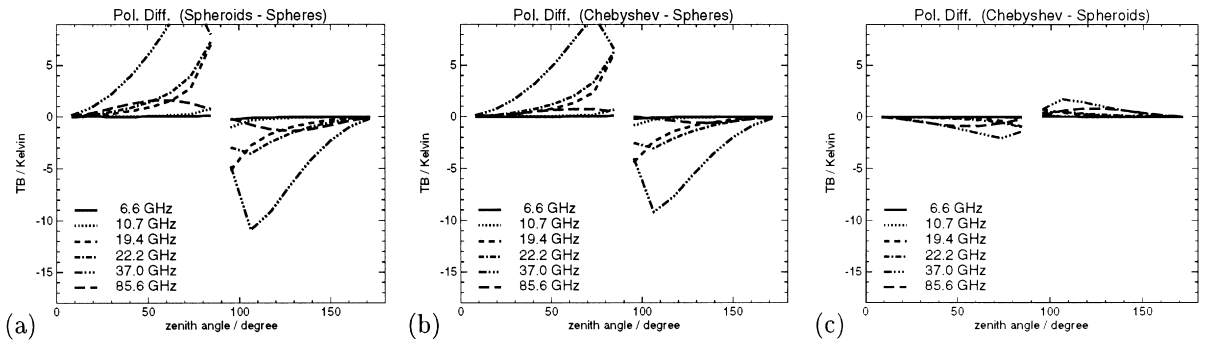
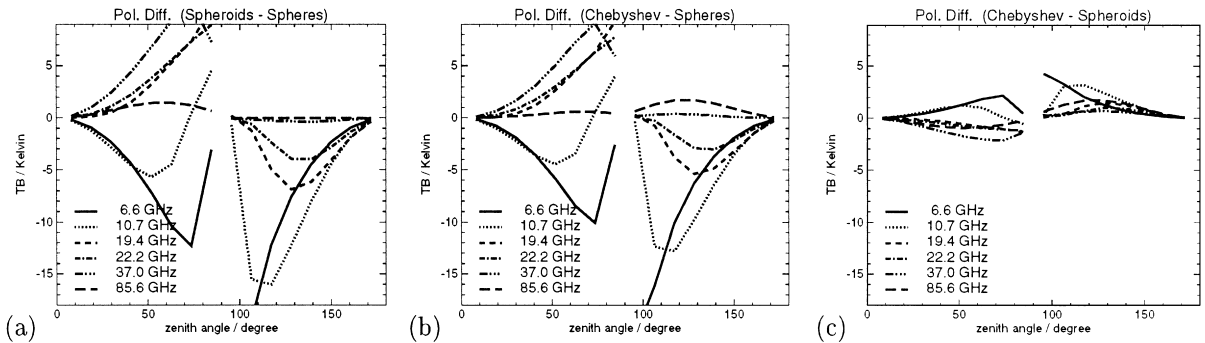Fig. 11. All settings as in Fig. 10, but with the ice particle layer only (no rain).

Fig. 12. All settings as in Fig. 6 (both layers, rain and ice), but with sea surface conditions at the lower boundary.

The combination of liquid and frozen precipitation in one calculation leads to a simple addition of the differences at upward directions (not shown here). Since the total PD at upwelling directions is not determined by the intense scattering contribution of ice particles alone, the effect of raindrop shape will be of interest for the remote sensing of precipitation. Polarization difference will be best suited for such applications because it is affected by all hydrometeor layers instead of only the uppermost ice particle layer.

The polarization results still depend on the surface emissivity. For a different distribution of intensity the changes of shape have different effects on the total PD. Fig. 12 gives the change in PD for the precipitating ice and rain layers over a sea surface (corresponding to Fig. 7). It is clear from Fig. 12c that the more realistic shapes described by the Chebyshev shapes add only little to the changes that can be obtained with a spheroid approximation, but the difference (up to an amount of 2 K for 25 mm/h rain rate) is still in the range of detection limits (usually $\Delta T < 1$ K) and may vary with higher and lower rain rates. The detailed results from calculations with varying rain rate, different viewing angles, and different surface conditions were subject of another study and will be published elsewhere.

5. Summary and conclusions

The differences for radiative transfer calculations using three different assumptions (spheres, spheroids and for the first time the realistic Chebyshev particle raindrop shape) for the geometry of hydrometeors are computed using a one-dimensional model. All hydrometeors have a rotational symmetric shape and are aligned to the vertical with their axis of rotation. The radiative transfer calculations were performed with three different types of lower boundary conditions in order to investigate the dependence of the observed changes on surface emissivity.

The results for oblate spheroids and oblate Chebyshev particles both show large deviations from those results obtained with spheres. The Chebyshev particles produce less changes than the spheroid approximation in nearly all tested cases. The variation of the particle shape produces the largest differences in intensity at nadir directions (up and downward), while the polarization signature increases with angle closer to the horizontal.

Liquid hydrometeors exhibit largest changes for 19, 22 and 37 GHz, while ice particles have a larger impact on 37 and 85 GHz. A combination of rain and ice layers add the effects induced by hydrometeor shape at upward directions, leaving the downward results to those obtained with the raining layer only.

The total change of the results when switching from the simplest approximation by spheres to the spheroid approximation, reaching values around 5 K, is crucial for exact forward calculations that are used to derive retrieval schemes. The additional slight variation of geometry when using Chebyshev geometry adds only little changes, but they are still large enough to be considered. However, the exact impact of particle shape on rainfall retrieval errors needs to be considered in a following study, which will also take into account a microphysical cloud model for the vertical structure of hydrometeor profiles rather than employing large rainshafts with fixed rain rate and size distribution. A detailed knowledge of hail particle shape and size distribution is crucial for the quality of forward model calculations.

References

[1] Crewell S, Ruprecht E, Simmer C. J Appl Meteorol 1991;30:1627.
[2] Solheim F, Godwin JR, Westwater ER, Han Y, Keihm SJ, Marsh K, Ware R. Radio Science 1998;33:393.
[3] van de Hulst HC. Light scattering by small particles. New York: Dover Publications, 1981:p.407.
[4] Pruppacher HR, Beard KV. Quart J Roy Meteorol Soc 1970;96:247.
[5] Pruppacher HR, Pitter RL. J Atmos Sci 1971;28:86.
[6] Chuang C, Beard KV. J Atmos Sci 1990;47:1374.
[7] Oguchi T. J Radio Res Lab 1960;7:467.

  [8] Oguchi T. J Radio Res Lab 1964;11:19.
  [9] Asano S, Yamamoto G. Appl Opt 1975;14:29.
 [10] Wu R, Weinman JA. J Geophys Res 1984;89(8):7170.
 [11] Haferman JL, Smith TF, Krajewski WF. J Quant Spectros Radiat Transfer 1997;58:379.
 [12] Czekala H, Simmer C. J. Quant Spectros Radiat Transfer 1998;60:365.
 [13] Haferman JL. In: Mishchenko MI, Hovenier JW, Travis LD, editors. Light scattering by nonspherical particles: theory, measurements, and applications. New York: Academic Press, 1999, in press.
 [14] Evans KF, Stephens GL. J Atmos Sci 1995;52:2041.
 [15] Evans KF, Stephens GL. J Atmos Sci 1995;52:2058.
 [16] Evans KF, Vivekanandan J. IEEE Trans Geosci Remote Sensing 1990;28:423.
 [17] Turk J, Vivekanandan J. In: Solomini D, editor. Microwave radiometry and remote sensing of the environment. Zeist, The Netherlands: VSP Press, 1995:p. 187–96.
 [18] Beard KV, Kubesh RJ, III HTO. J Atmos Sci 1991;48:698.
 [19] Beard KV, Chuang C. J Atmos Sci 1987;44:1509.
 [20] Andsager K, Beard KV, Laird NF. J Atmos Sci 1999, submitted for publication.
 [21] Simmer C. Satellitenfernerkundung hydrologischer Parameter der Atmosphäre mit Mikrowellen. Verlag Dr. Kovac. 1994:p.314.
 [22] Czekala H. Geophys Res Lett 1998;25:1669.
 [23] Tsang L, Kong JA, Shin RT. Theory of microwave remote sensing. New York: Wiley, 1985:p.613.
 [24] Liebe HJ. Radio Sci 1985;20:1069.
 [25] Liebe HJ, Hufford GA, Cotton MG. AGARD 52nd Specialists Meeting of the Electromagnetic Wave Propagation Panel, Palma de Mallorca, Spain, May 17–21, 1993.
 [26] Ulaby FT, Moore RK, Fung AK. Microwave remote sensing, active and passive, Vol. 3. Reading, MA: Addison-Wesley, 1986:p.1098.
 [27] Mie G. Ann Phys 1908;25:377.
 [28] Mishchenko MI, Travis LD, Mackowski DW. J Quant Spectros Radiat Transfer 1996;55:535.
 [29] Rother T, Schmidt K. In: Kong J, editor. Progress in electromagnetic research, PIER 17. Cambridge, Massachusetts, USA: EMV Publishing, 1997:p. 91–183.
 [30] Rother T. J Quant Spectrosc Radiat Transfer 1998;60:335.
 [31] Mugnai A, Wiscombe WJ. Appl Opt 1986;25:1235.
 [32] Rother T, Havemann S, Schmidt K. J. Electromagn Waves Appl 1999, in press.
 [33] Marshall JS, Palmer W. J Meteorol 1948;5:165.